Structural Engineering and Mechanics, Vol. 3, No. 5 (1995) 511-525
DOI: http://dx.doi.org/10.12989/sem.1995.3.5.511

In-plane free vibrations of catenary arches with unsymmetric axes

James F. Wilson†

Department of Civil Engineering, Duke University, Durham, NC 27708-0287, U.S.A.

Byoung Koo Lee†

Department of Civil Engineering, Wonkwang University, Iri, Junbuk 570-749, Korea

Abstract. The differential equations governing in-plane free vibrations of the elastic, catenary arch with rotatory inertia are derived in Cartesian coordinates. Frequencies and mode shapes are computed numerically for such arches with unsymmetric axes, for both clamped-clamped and hinged-hinged end constraints. The lowest four natural frequency parameters are reported, with and without rotatory inertia, as a function of three nondimensional system parameters; the span to cord length ratio e, the slenderness ratio s, and the rise to cord length ratio f. Experimental measures of frequencies and mode shapes for several laboratory-scale catenary models serve to validate the theoretical results.

Key words: catenary arch; determinant search method; free vibration; mode shape; rotatory inertia; Runge-Kutta method; unsymmetric axis.

1. Introduction

Studies on the free vibrations of linearly elastic arches of various shapes have been reported for more than three decades. Such studies were critically reviewed by Laura and Maurizi (1987). Background material for the current study was summarized by Lee and Wilson (1989). Briefly, such works included studies of noncircular arches with predictions of the lowest frequency in flexure by Romanelli and Laura (1972), and in extension by Wang (1972), and Wang and Moore (1973): studies of circular arches with predictions of higher flexural frequencies by Wung (1967), Wolf (1971), Veletsos, *et al.* (1972), and Austin and Veletsos (1973); and studies showing the effects of transverse shear and rotatory inertia on free vibration frequencies of circular arches by Irie, *et al.* (1983) and Davis, *et al.* (1972). Experimental studies to validate predicted arch frequencies and mode shapes are rare, although recent such studies on selected arches were reported by Perkins (1990) and by Lee and Wilson (1989).

This paper has two main purposes: (1) to present for the first time the equations for free, planar vibrations of arches with unsymmetric axes, variable curvature, and rotatory inertia, where all equations are derived in Cartesian rather than in polar coordinates; and (2) to illustrate the numerical solutions to these newly-derived equations for a broad class of catenary arches. In most previous works on arch vibrations, polar coordinates were employed and the arch shapes

† Professor

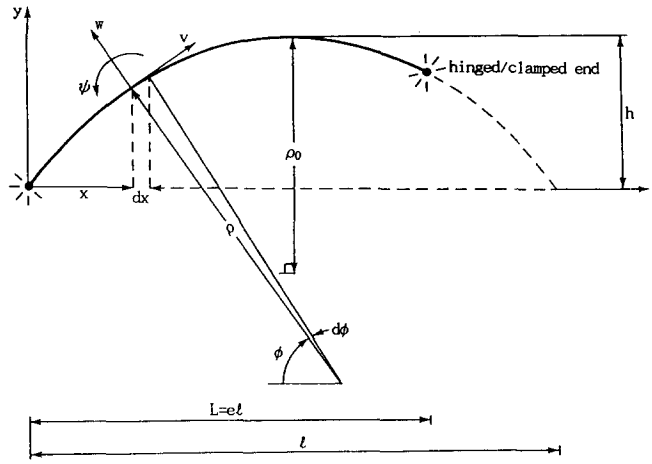

Fig. 1 Geometry of the catenary arch and its defining variables.

were either circular, parabolic, sinusoidal, or elliptic. The two exceptions were the works of Volterra and Morell (1961) and Romanelli and Laura (1972) who predicted only the fundamental frequencies for catenary arches hinged at both ends. The results presented herein extend significantly these latter two works. That is, using the Cartesian formulation together with highly efficient and convergent numerical methods, the free, in-plane vibration frequencies and mode shapes, with and without rotatory inertia, are investigated for catenary arches. Such numerical results are presented for clamped-clamped and hinged-hinged end constraints. The lowest four non-dimensional frequency parameters are shown as functions of three system parameters: the arch span to cord length ratio e, the slenderness ratio s, and the rise to cord length ratio f. The computed results are then complemented with experimental results measured from laboratory-scale models of catenary arches.

2. Mathematical model

The geometry and nomenclature of the catenary arch are shown in Fig. 1. The geometric variables are defined as follows.

L span length
l cord length
h rise
ρ_0 radius of curvature at the crown
e span length to cord length ratio, $e=L/l$
x, y rectangular coordinates
v, w, ψ displacements and rotation of cross-section
ρ radius of curvature
ϕ inclination of radius of curvature with x-axis

The shape of catenary is expressed in terms of (l, h, ρ_0) and the coordinate x in the range from $x=0$ to $x=L(=el)$. That is,

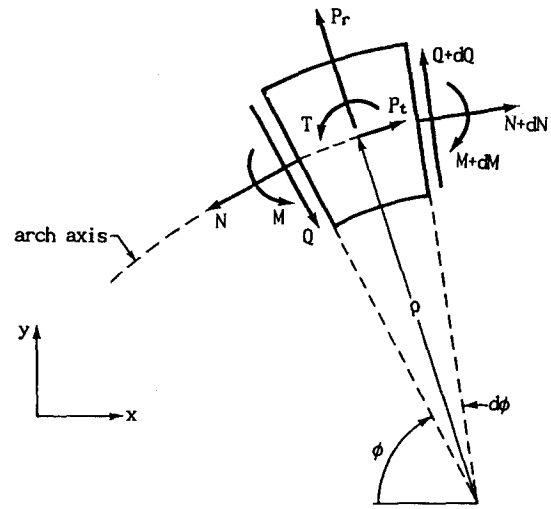

Fig. 2 Loads on a small arch element.

$$y=h+\rho_0-\rho_0\cos h\left(\frac{x-0.5l}{\rho_0}\right), \qquad 0\le x\le L \tag{1}$$

The arch is supported by either hinged or clamped ends.

A small element of the arch is shown in Fig. 2 in which are defined the positive directions for the axial force N, the shear force Q, the bending moment M, the radial inertia force P_r, the tangential inertia force P_t, and the rotatory inertia couple T. Treating the inertia forces and the inertia couple as equivalent static quantities, the three equations for "dynamic equilibrium" of the element are

$$dN/d\phi+Q+\rho P_t=0 \tag{2}$$

$$dQ/d\phi-N+\rho P_r=0 \tag{3}$$

$$\rho^{-1}dM/d\phi-Q-T=0 \tag{4}$$

The equations that relate N, M and ψ to the displacements w and v (Borg 1959) are

$$N=EA\rho^{-1}[(v^{i}+w)+r^2\rho^{-2}(w^{ii}+w)] \tag{5}$$

$$M=-EAr^2\rho^{-2}(w^{ii}+w) \tag{6}$$

$$\psi=\rho^{-1}(w^{i}-v) \tag{7}$$

where E is Young's moduls, A is the cross-sectional area, r is the radius of gyration of the cross-section, and (i) is the operator $d/d\phi$.

The arch is assumed to be in harmonic motion, or each coordinate is proportional to $\sin(\omega t)$ where ω is the circular frequency and t is time. The inertia loadings per unit arc length are then

$$P_r=m\omega^2 w \tag{8}$$

$$P_t=m\omega^2 v \tag{9}$$

$$T=m\omega^2 r^2 \psi=m\omega^2 r^2 \rho^{-1}(w^i-v) \tag{10}$$

where m is mass per unit arc length.

When Eqs. (5) and (6) are differentiated once, the results are

$$\begin{aligned} dN/d\phi=EA\rho^{-1}[(v^{ii}+w^i)+r^2\rho^{-2}(w^{iii}+w^i) \\ -\rho^{-1}\rho^i(v^i+w)-3r^2\rho^{-3}\rho^i(w^{ii}+w)] \end{aligned} \tag{11}$$

$$dM/d\phi=-EAr^2\rho^{-2}[(w^{iii}+w^i)-2\rho^{-1}\rho^i(w^{ii}+w)] \tag{12}$$

When Eqs. (10) and (12) are substituted into Eq. (4), then

$$\begin{aligned} Q=\rho^{-1}dM/d\phi-RT \\ =-EAr^2\rho^{-3}[(w^{iii}+w^i)-2\rho^{-1}\rho^i(w^{ii}+w)]-Rm\omega^2 r^2\rho^{-1}(w^i-v) \end{aligned} \tag{13}$$

where the index R is defined as follows.

$$R=1 \text{ if the rotatory inertia couple } T \text{ is included} \tag{14a}$$

$$R=0 \text{ if } T \text{ is excluded} \tag{14b}$$

The following equation is obtained by differentiating Eq. (13).

$$\begin{aligned} dQ/d\phi=-EAr^2\rho^{-3}[(w^{iv}+w^{ii})-5\rho^{-1}\rho^i(w^{iii}+w^i) \\ +2\rho^{-1}(4\rho^{-1}\rho^{i2}-\rho^{ii})(w^{ii}+w)] \\ -Rm\omega^2 r^2\rho^{-1}[(w^{ii}-v^i)-\rho^{-1}\rho^i(w^i-v)] \end{aligned} \tag{15}$$

From Fig. 1, it is seen that the arch inclination is related to the coordinate x as follows.

$$\phi=\frac{\pi}{2}-\tan^{-1}\left[\frac{dy}{dx}\right]=\frac{\pi}{2}-\tan^{-1}\left[-\sin h\left(\frac{x-0.5l}{\rho_0}\right)\right] \tag{16}$$

When Eq. (16) is differentiated, the result is

$$d\phi=\frac{dx}{\rho_0 \cos h\left[\frac{x-0.5l}{\rho_0}\right]} \tag{17}$$

Define the following two arch parameters.

$$\varepsilon_1=\cos h\left[\frac{x-0.5l}{\rho_0}\right] \tag{18a}$$

$$\varepsilon_2=\sin h\left[\frac{x-0.5l}{\rho_0}\right] \tag{18b}$$

From Eq. (17), and with Eqs. (18), the following differential operators are obtained.

$$\frac{d}{d\phi}=\rho_0\varepsilon_1\frac{d}{dx} \tag{19a}$$

$$\frac{d^2}{d\phi^2}=\frac{d}{d\phi}\left[\frac{d}{d\phi}\right]=\rho_0\varepsilon_1\left[\rho_0\varepsilon_1\frac{d^2}{dx^2}+\varepsilon_2\frac{d}{dx}\right] \tag{19b}$$

$$\frac{d^3}{d\phi^3}=\frac{d}{d\phi}\left[\frac{d^2}{d\phi^2}\right]=\rho_0\varepsilon_1\left[\rho_0^2\varepsilon_1^2\frac{d^3}{dx^3}+3\rho_0\varepsilon_1\varepsilon_2\frac{d^2}{dx^2}+(2\varepsilon_1^2-1)\frac{d}{dx}\right] \tag{19c}$$

$$\frac{d^4}{d\phi^4}=\frac{d}{d\phi}\left[\frac{d^3}{d\phi^3}\right]$$

$$=\rho_0\varepsilon_1\left[\rho_0^3\varepsilon_1^3\frac{d^4}{dx^4}+6\rho_0^2\varepsilon_1^2\varepsilon_2\frac{d^3}{dx^3}+\rho_0\varepsilon_1(11\varepsilon_1^2-7)\frac{d^2}{dx^2}+\varepsilon_2(6\varepsilon_1^2-1)\frac{d}{dx}\right] \tag{19d}$$

The radius of curvature ρ at any point of the catenary is expressed as follows, where Eq. (18a) is used.

$$\rho=\frac{\left[1+\left(\frac{dy}{dx}\right)^2\right]^{3/2}}{\left[\frac{d^2y}{dx^2}\right]}=\rho_0\varepsilon_1^2 \tag{20}$$

Also, ρ^i, ρ^{ii} can be expressed in terms of x by using Eq. (20) with Eqs. (19a) and (19b). That is

$$\rho^i=\frac{d\rho}{d\phi}=\rho_0\varepsilon_1\frac{d}{dx}(\rho_0\varepsilon_1^2)=2\rho_0\varepsilon_1^2\varepsilon_2 \tag{21}$$

$$\rho^{ii}=\frac{d\rho^i}{d\phi}=\rho_0\varepsilon_1\frac{d}{dx}(2\rho_0\varepsilon_1^2\varepsilon_2)=2\rho_0\varepsilon_1^2(3\varepsilon_1^2-2) \tag{22}$$

Now cast the differential equations of free vibration for the arch into non-dimensional form by introducing the following non-dimensional parameters.

$$\bar{x}=x/l,\ \bar{y}=y/l \tag{23}$$

$$\xi=w/l,\ \eta=v/l \tag{24}$$

$$f=h/l,\ g=l/\rho_0 \text{ (shape factors)} \tag{25}$$

$$s=l/r \text{ (slenderness ratio)} \tag{26}$$

Here the coordinates (x, y), the displacements (w, v), and the arch rise h are normalized by the catenary cord length, l. The non-dimensional equation of the catenary is defined by the shape parameters f and g as

$$\bar{y}=f+g^{-1}-g^{-1}\cosh[g(\bar{x}-0.5)] \tag{27a}$$

Substituting $\bar{x}=1$ and $\bar{y}=0$ into Eq. (27a) leads to

$$fg-\cosh(0.5g)+1=0 \tag{27b}$$

For a given catenary shape factor f, the corresponding g value can be obtained by Eq. (27b) by using the bisection method, the method used herein.

When Eqs. (5), (8) and (15) together with Eqs. (19)-(26) are used in Eq. (3), the result is Eq. (28). Also, when Eqs. (9), (11) and (13) are combined with Eq. (2), the result is Eq. (29). That is

$$\xi''''=a_1\xi'''+(a_2+Ra_3C_i^2)\xi''+(a_4+Ra_5C_i^2)\xi'+(a_6+a_7C_i^2)\xi+(a_8+Ra_9C_i^2)\eta'+Ra_{10}C_i^2\eta \tag{28}$$

$$\eta''=a_{11}\xi''+(a_{12}+Ra_{13}C_i^2)\xi'+a_{14}\xi+a_{15}\eta'+(a_{16}+Ra_{17})C_i^2\eta \tag{29}$$

In these latter two equations, $(')$ is the operator $d/d\bar{x}$, and the constants are as follows.

$$a_1=4g\lambda_1\lambda_2 \tag{30a}$$

$$a_2=-g^2(\lambda_2^2+1) \tag{30b}$$

$$a_3=-s^{-2}\lambda_3^2 \tag{30c}$$

$$a_4=-g^3\lambda_1\lambda_2^3(6\lambda_1^2-17) \tag{30d}$$

$$a_5=s^{-2}g\lambda_1\lambda_3 \tag{30e}$$

$$a_6=-g^4\lambda_2^4(s^2g^{-2}\lambda_3^4+20\lambda_3^2-23) \tag{30f}$$

$$a_7=\lambda_3^4 \tag{30g}$$

$$a_8=-s^{-2}g\lambda_3 \tag{30h}$$

$$a_9=s^{-2}g\lambda_3 \tag{30i}$$

$$a_{10}=-2s^{-2}g^2\lambda_1 \tag{30j}$$

$$a_{11}=2s^{-2}g^2\lambda_1\lambda_2^4 \tag{30k}$$

$$a_{12}=-s^{-2}g^3\lambda_2^5(s^2g^{-2}\lambda_3^4-2\lambda_1^2) \tag{30l}$$

$$a_{13}=s^{-4}g\lambda_2 \tag{30m}$$

$$a_{14}=2s^{-2}g^4\lambda_1\lambda_2^6(s^2g^{-2}\lambda_3^4+1) \tag{30n}$$

$$a_{15}=g\lambda_1\lambda_2 \tag{30o}$$

$$a_{16}=-s^{-2}\eta_3^2 \tag{30p}$$

$$a_{17}=-s^{-4}g^2\lambda_2^2 \tag{30q}$$

$$\lambda_1=\sinh[g(\bar{x}-0.5)] \tag{31a}$$

$$\lambda_2=\operatorname{sech}[g(\bar{x}-0.5)] \tag{31b}$$

$$\lambda_3=\cosh[g(\bar{x}-0.5)] \tag{31c}$$

The non-dimensional frequency parameter is defined as

$$C_i=\omega_i r^{-1}l^2(m/EA)^{1/2}=\omega_i s l(\gamma/E)^{1/2},\ i=1,\ 2,\ 3,\ 4,\cdots \tag{32}$$

where γ is mass density and i is mode number.

At a hinged end ($x=0$ or $x=L$), the boundary conditions are $w=v=M=0$ and these relations can be expressed in nondimensional form as

$$\xi=0,\ \text{at left end } (\bar{x}=0) \text{ or right end } (\bar{x}=e) \tag{33}$$

$$\eta=0,\ \text{at left end } (\bar{x}=0) \text{ or right end } (\bar{x}=e) \tag{34}$$

$$\xi''+g\lambda_1\lambda_2\xi'=0,\ \text{at left end } (\bar{x}=0) \text{ or right end } (\bar{x}=e) \tag{35}$$

At a clamped end ($x=0$ or $x=L$), the boundary conditions are $w=v=\psi=0$ and these relations can be expressed as the non-dimensional form as

$$\xi=0,\ \text{at left end } (\bar{x}=0) \text{ or right end } (\bar{x}=e) \tag{36}$$

$$\eta=0,\ \text{at left end } (\bar{x}=0) \text{ or right end } (\bar{x}=e) \tag{37}$$

$$\xi'=0, \text{ at left end } (\bar{x}=0) \text{ or right end } (\bar{x}=e) \tag{38}$$

3. Numerical results and discussion

A FORTRAN computer program was written to calculate C_i, $\xi=\xi_i(\bar{x})$, $\eta=\eta_i(\bar{x})$. The numerical methods similar to those described by Leonard (1988) and Lee and Wilson (1989) were used to solve the differential Eqs. (28) and (29), subject to the end constraint Eqs. (33)-(35) or (36)-(38). For the sake of completeness, this numerical procedure is summarized as follows.

(1) Specify $R(=0$ or 1), the arch geometry (f, e, s), and the set of three homogeneous boundary constraints which are either Eqs. (33)-(35) or Eqs. (36)-(38).
(2) Consider the sixth order system, Eqs. (28) and (29), as three initial value problems whose initial values are the three homogeneous boundary constraints $\bar{x}=0$, as chosen in Step 1. Then assume a trial frequency parameter C_i in which the first trial value is zero.
(3) Using the Runge-Kutta method, integrate Eqs. (28) and (29) from $\bar{x}=0$ to $\bar{x}=e$. Perform three separate integrations, one for each of the three chosen boundary constraints.
(4) From the Runge-Kutta solution, evaluate at $\bar{x}=e$ the determinant D of the coefficient matrix for the chosen set of three homogeneous boundary conditions. If $D=0$, then the trial value of C_i is an eigenvalue. If $D\neq 0$, then increment C_i and repeat the above calculations.
(5) Repeat Steps 3 and 4 and note the sign of D in each iteration. If D changes sign between two consecutive trials, then the eigen value lies between these last two trial values of C_i.
(6) Use the Regula-Falsi method to compute the advanced trial C_i based on its two previous values.
(7) Terminate the calculations and print the value of C_i and the corresponding mode shapes when the convergence criteria are met.

For these studies, suitable convergence of solutions was obtained for an increment of $\Delta\bar{x}=e/100$. The convergence criterion was that C_i solutions obtained with a more crude increment of $e/30$ agreed with those obtained with the $e/100$ increment to within three significant figures. The numerical results, given in Tables 1-3 and Figs. 3-6, are now discussed.

The first series of numerical studies are shown in Table 1. These studies served as an approximate check on the analysis presented herein. For comparison purposes, finite element solutions based on the commercial package SAP90 were used to compute the first four frequency parameters C_i for two cases: a hinged-hinged arch with $f=0.1$, $e=0.75$, and $s=50$; and a clamped-clamped

Table 1 Comparison of results between finite element solutions (SAP 90) and this study

Geometry of arch	i	Frequency parameters, C_i	
		SAP 90	This study ($R=1$)
Both hinged ends	1	38.31	38.07
$f=0.1$, $e=0.75$	2	65.93	65.41
$s=50$	3	151.20	147.11
	4	207.67	207.34
Both clamped ends	1	73.10	72.05
$f=0.3$, $e=0.75$	2	130.51	128.80
$s=100$	3	181.53	179.93
	4	256.43	252.11

Table 2 The effect of rotatory inertia on frequency

Geometry of arch		i	Frequency parameter, C_i		Effect(%)*
			$R=0$ (A)	$R=1$ (B)	
Both hinged end	$f=0.1$	1	38.20	38.07	−0.34
	$e=0.75$	2	66.24	65.41	−1.27
	$s=50$	3	151.44	147.11	−2.94
		4	207.57	207.34	−0.11
	$f=0.3$	1	46.32	46.23	−0.19
	$e=0.75$	2	107.79	107.30	−0.46
	$s=100$	3	166.51	166.27	−0.14
		4	204.21	202.26	−0.96
Both clamped end	$f=0.1$	1	49.39	49.19	−0.41
	$e=0.75$	2	103.36	101.85	−1.48
	$s=50$	3	205.73	199.30	−3.23
		4	207.70	207.40	−0.14
	$f=0.3$	1	72.21	72.05	−0.22
	$e=0.75$	2	129.23	128.80	−0.33
	$s=100$	3	180.57	179.93	−0.36
		4	254.69	252.11	−1.02

*Effect (%)=(B−A)×100/B

Table 3 Comparison of computed and measured results ($f=0.25$, $e=0.75$, $s=218$, $R=1$)

End constraint	Mode no. i	Theory		Experiment	% Deviation
		C_i	f_i (Hz)	f_i (Hz)	
Hinged-hinged	1	51.62	477.23	430.	−9.9
	2	119.13	1101.36	870.	−21.0
	3	221.24	2045.36	(1130.);1790.	(−45.);−12.5
	4	311.60	2880.74	—	—
Clamped-clamped	1	80.72	746.25	640.	−14.2
	2	154.55	1428.81	1330.	6.9
	3	276.80	2559.02	2180.	−14.8
	4	314.56	2908.11	3340.	+14.9

configuration with $f=0.3$, $e=0.75$, and $s=100$. The results showed that 100 three-dimensional finite beam elements (with the omission of the shear areas associated with transverse shear loadings) were necessary to match within a tolerance of 2% values of C_i computed by solving the governing differential Eqs. (28) and (29) in which rotatory inertia was included ($R=1$).

All of the numerical results that follow are based on the analysis reported herein. In Table 2, it is apparent that the frequencies increase, respectively, as the end constraints increase from hinged to clamped, other parameters remaining the same. Further, the effect of rotatory inertia is to always depress the natural frequencies. In these examples, for the lowest frequency ($i=1$), this depression is less than 0.5%. Also, in most of these examples there is a trend of an increased depression in frequency (3.23% at the most) when arches of like geometry but with increasing end constraint are compared.

It is shown in Fig. 3, for which $f=0.3$, $s=100$, and $R=1$, that the frequency parameters C_i ($i=1, 2, 3, 4$) decrease as the span to cord length ratio e is increased. This holds true for both

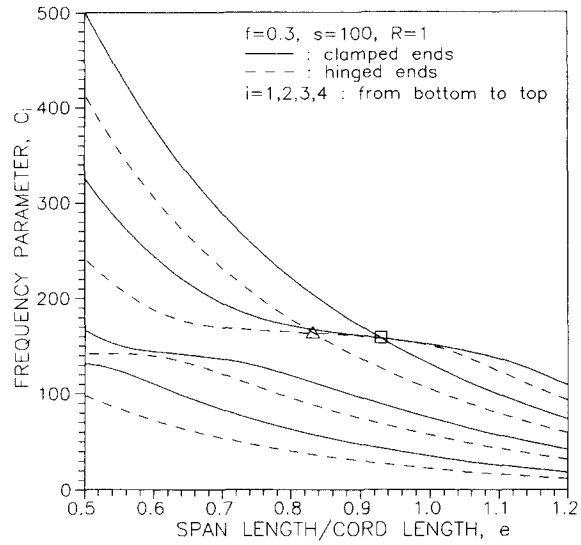

Fig. 3 The effect of e with $f=0.3$, $s=100$ and $R=1$ on C_i for hinged-hinged and clamped-clamped arches.

the hinged end and clamped end arches. Further, it is observed for these unsymmetric arch configurations that two modes can exist at a single frequency, a phenomena that was previously observed only for symmetric arch configurations (Lee and Wilson 1989). For the hinged-hinged arch, the third and fourth modes have the same frequency at $C_3=C_4=164.0$ and $e=0.831$ (marked △). Also, for the clamped-clamped arch, the third and fourth modes have the same frequency at $C_3=C_4=158.4$ and $e=0.929$ (marked as □ in Fig. 3).

It is shown in Fig. 4, for which $f=0.3$, $e=0.75$, and $R=1$, that the frequency parameters increase, and in most cases approach a horizontal asymptote, as the slenderness ratio s is increased.

It is shown in Fig. 5, for which $e=1$, $s=100$, and $R=1$, that several of the frequency parameters reach a peak as the rise to cord length ratio f is increased. Further, four pairs of lines cross, which shows that two mode shapes may exist at the same frequency. That is, the lowest two modes may exist where $C_1=C_2$ at $f=0.05$ for the hinged arch, and at $f=0.08$ for the clamped arch. Also, the third and fourth modes may exist where $C_3=C_4$ at $f=0.2$ for the hinged arch and at $f=0.26$ for the clamped arch.

Shown in Fig. 6 are the computed frequency parameters C_i ($i=1, 2, 3, 4$) and their corresponding mode shapes for both hinged and clamped end configurations for which $f=0.25$, $e=0.75$, $s=218$, and $R=1$. These arch parameters are those chosen for the experimental arches discussed in the next section. These mode shapes are defined as A type or B type, analogous to the mode shapes in symmetric arch geometries in which the A type is the asymmetric mode and the B type is the symmetric mode. At the △ and □ points in Fig. 3, either the A or B type mode may exist. The mode shapes for the present unsymmetric arch geometries are defined quantitatively as follows.

For the hinged-hinged arch:

$$\text{A type: } \xi''_{\bar{x}=0}\cdot\xi''_{\bar{x}=e}<0$$

$$\text{B type: } \xi''_{\bar{x}=0}\cdot\xi''_{\bar{x}=e}>0$$

For the clamped-clamped arch:

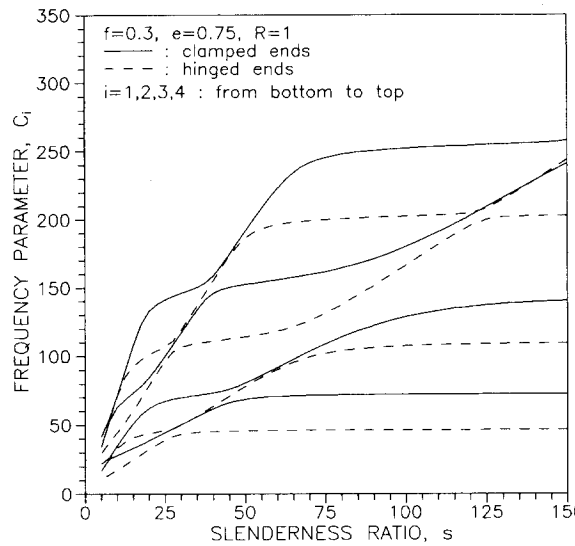

Fig. 4 The effect of s with $f=0.3$, $e=0.75$ and $R=1$ on C_i for hinged-hinged and clamped-clamped arches.

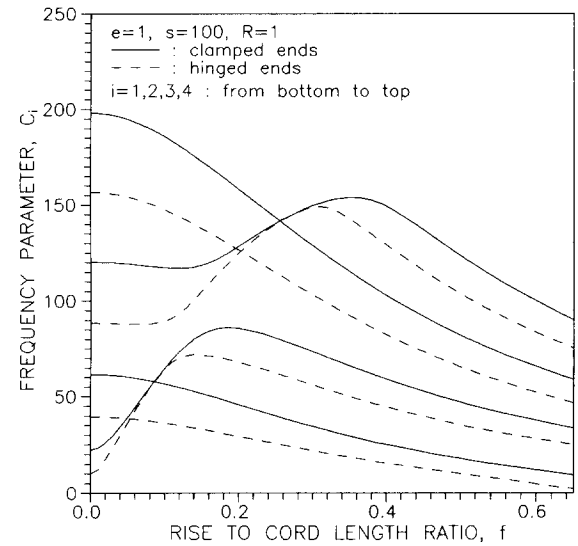

Fig. 5 The effect of f with $e=1$, $s=100$ and $R=1$ on C_i for hinged-hinged and clamped-clamped arches.

A type: $\xi'''_{\bar{x}=0} \cdot \xi'''_{\bar{x}=e} > 0$

B type: $\xi'''_{\bar{x}=0} \cdot \xi'''_{\bar{x}=e} < 0$

4. Experimental results and discussion

Two laboratory-scale catenary arches, a hinged-hinged and a clamped-clamped configuration,

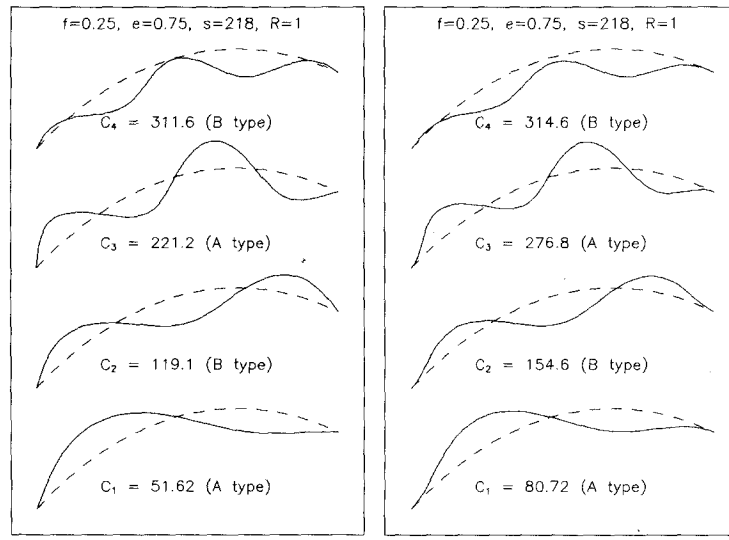

Fig. 6 Mode shapes with $f=0.25$, $e=0.75$, $s=218$ and $R=1$ for hinged-hinged and clamped-clamped arches.

were designed and tested to determine their lowest few natural frequencies and their corresponding mode shapes. The experimental setup showing the clamped-clamped model only is shown in Fig. 7. The main purpose of these experiments was to validate the proposed mathematical model and typical numerical solutions predicted herein.

The experimental models were bent from aluminum bar stock to the catenary shape with (x, y) coordinates described by Eq. (1). Here, ρ_0, the crown radius of curvature, was computed from Eq. (25) with g computed from Eq. (27b). The geometric arch parameters were: $L=30$ cm, $l=40$ cm, $h=10$ cm; and cross section was rectangular: 2.54 cm wide and 0.635 cm thick. With these dimensions, $\rho_0=21.49$ cm and the nondimensional arch parameters, computed from Eqs. (26) and (27), were $f=0.25$, $e=0.75$, and $s=218.0$.

As discussed above, the first four predicted frequency parameters C_i and their respective mode shapes for the experimental arches are presented in Fig. 6. Using these values of C_i with Eq. (32) and the material properties of the experimental arches, the experimental arch frequencies f_i (Hz) may be predicted. The material properties of the aluminum arches were: $E=6.89\times10^{10}$ N/m^2 and $\gamma=2680$ kg/m^3. It follows that $f_i=\omega_i/(2\pi)=9.245C_i$ Hz, and these numerical values are listed in Table 3.

The experimental setup is shown in Fig. 7. The procedures for measuring frequencies and mode shapes follow those discussed in detail by Lee and Wilson (1989); and the methods for reducing data follow those discussed by Ewins (1985). For the sake of completeness, those procedures and methods are summarized. At each end, the arch was either hinged or clamped to a steel connection attached to a 50 kg concrete block. Each block "floated" on a soft rubber pad to achieve vibration isolation. Including the end points, 17 reference points were chosen along the hinged arch, and 15 along the clamped arch. As shown in Fig. 7, a miniature accelerometer sensitive only to radial acceleration (in-plane bending vibrations) was affixed to the underside of the arch at an interior reference point. A small hammer fitted with a miniature accelerometer sensitive to accelerations in the direction of impact, was used to strike each of the reference

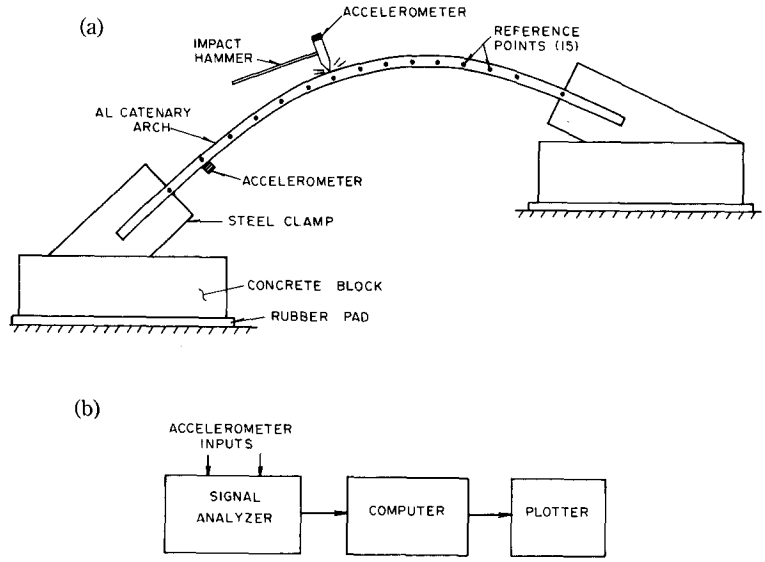

Fig. 7 (a) The experimental setup
(b) The modal analysis system.

points, excluding the end points. The two acceleration time histories measured at each strike were received by a signal analyzer (Model SD380Z, Scientific Atlanta Corp.) and then processed by a microcomputer using a fast Fourier transform (FFT) analyzer. Using all of these data, two types of computations were then performed: (1) the frequency dependent transfer function, defined as the ratio of the magnitude of the FFT of the arch acceleration to the magnitude of the FFT of the hammer acceleration; and (2) the mode shape that corresponded to the frequency at each significant peak of the transfer function. The experimental results are summarized in Fig. 8, Fig. 9, and Table 3.

Shown in Fig. 8 are the transfer functions for the hinged-hinged and clamped-clamped models. The frequencies for the major peaks of these plots are listed in Table 3. For each of these frequencies, the measured envelopes of the mode shapes are shown in Fig. 9. These shapes are somewhat crude since the software simply connects the measured peak node point radial displacements with straight lines.

For the hinged arch, the three measured frequencies that occurred at the first, second, and fourth peak of the transfer function, Fig. 8a, were 430, 870, and 1790 Hz, respectively. The measured mode shapes for these respective frequencies, Fig. 9a, agree reasonably well with the predicted shapes shown in Fig. 6. These three frequencies average about 14% less than the predicted values. Natural damping present in the experimental system but absent in the theoretical model contributes to the depression of the measured frequencies. The inevitable looseness of the end hinges and the difficulty in maintaining in-plane hammer strikes undoubtedly lead to out-of plane vibrations, "noise" in the transfer function, and the inability to achieve meaningful results for frequencies higher than third. Some or all of these factors probably account for the third significant peak in Fig. 8a which occurs at 1130 Hz. At this frequency, a mode shape similar to that at 1790 Hz was measured (Fig. 8a), but not predicted. However, the higher value of the transfer function near zero frequency is easily explained: it is undoubtedly due to the rocking response of the 50 kg concrete blocks which rested on rubber pads at the ends of the arch. This assembly has the relatively low natural frequency of about 2 Hz.

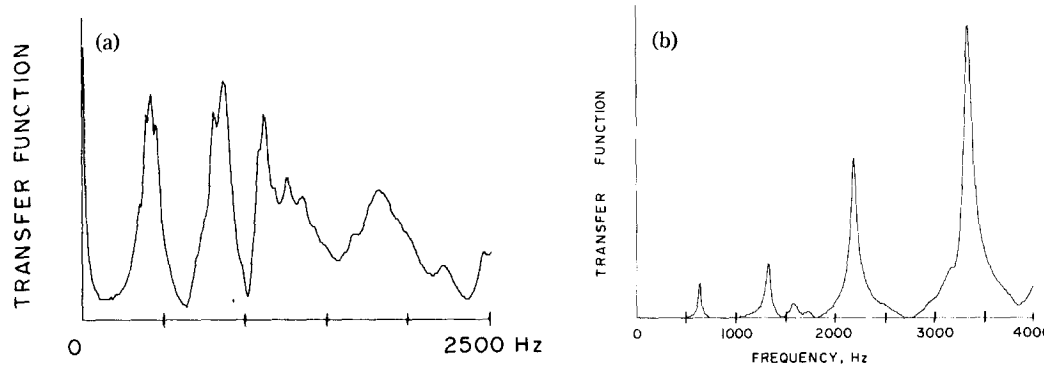

Fig. 8 Measured transfer function of acceleration for (a) the hinged-hinged arch (b) the clamped-clamped arch.

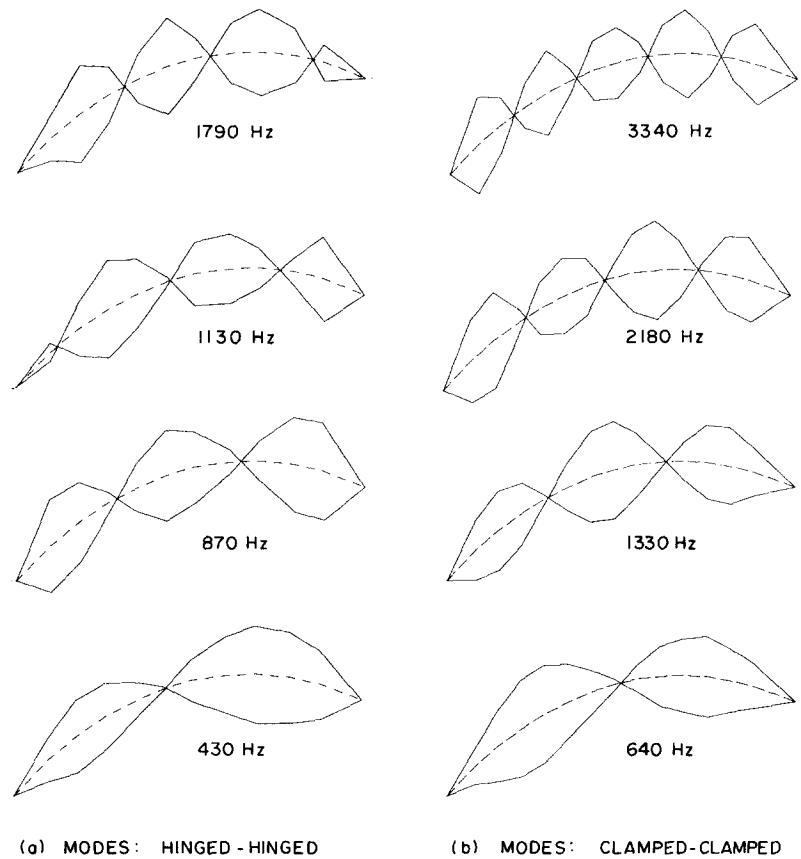

Fig. 9 Measured frequencies and mode shapes for the experimental arches.

For the clamped arch, the ideal end constraints were more nearly achieved and this is reflected in the rather "clean" transfer function shown in Fig. 8b. As shown in Table 3, the frequencies occurring at these consecutive peaks are within 15% of the predicted values. Again, because of the straight-line software extrapolation of mode shape data, the ends of this arch do not approach the actual zero slope relative to the underformed arch (the dashed line). However, at points further than about two reference points from the ends, the mode shapes are approximately in agreement with the computed ones shown in Fig. 6.

5. Conclusions

By employing the governing equations in Cartesian coordinates, the numerical methods for calculating the free vibration, in-plane frequencies and mode shapes for catenary arches with unsymmetric axes were found to be especially robust and reliable over a wide and practical range of arch parameters. For hinged ends and also for clamped ends, the numerical results showed that neither pure symmetric nor pure asymmetric mode shapes exist; but such shapes that nearly fit these categories were identified and precisely defined. Further, at several critical combinations of system parameters, two mode shapes were found to exist at a single natural frequency, a phenomenon previously observed for circular arches. The inclusion of rotatory inertia was found to depress the natural frequencies, particularly the higher ones, but in no case was this depression higher than 4%. The experimental studies of hinged-hinged and clamped-clamped laboratory model arches showed that most of the measured frequencies were within 15% of the predicted ones, and that measured and predicted mode shapes were similar. Thus, these experiments served to validate the methods of analysis.

Acknowledgements

The authors thank Mrinmay Biswas for the use of his experimental modal analyzer system and Arun Pandey for his able assistance with the experiments.

References

Austin, W. J. and Veletsos, A. S. (1973), "Free vibration of arches flexible in shear", *Journal of the Engineering Mechanics Division,* **99**(EM4), 735-753.

Borg, S. F. and Gennaro, J. J. (1959), *Advanced structural analysis,* Van Nostrand, Princeton, New Jersey.

Davis, R., Henshell, R. D. and Warburton, G. B. (1972), "Constant curvature beam finite elements for in-plane vibration", *Journal of Sound and Vibration,* **25**, 561-576.

Ewins, D. J. (1985), *Modal testing: theory and practice,* John Wiley, New York.

Irie, T., Yamada, G. and Tanaka, K. (1983), "Natural frequencies of in-plane vibration of arcs", *Journal of Applied Mechanics,* **50**, 449-452.

Laura, P. A. A. and Maurizi, M. J. (1987), "Recent research in the vibration of arch-type structures", *Shock and Vibration Digest,* **19**(1), 6-9.

Lee, B. K. and Wilson, J. F. (1989), "Free vibrations of arches with variable curvature", *Journal of Sound and Vibration,* **136**(1), 75-89.

Leonard, J. W. (1988), *Tension structures,* McGraw-Hill Book Company, 300-304.

Perkins, N. C. (1990), "Planar vibration of an elastica arch: theory and experiment", *Journal of Vibration and Acoustics,* **112**, 374-379.

Romanelli, E. and Laura, P. A. A. (1972), "Fundamental frequencies of non-circular, elastic, hinged arcs", *Journal of Sound and Vibration,* **24**(1), 17-22.
Veletsos, A. S. and Austin, W. J., Pereira, C. A. L. and Wung, S. J. (1972), "Free in-plane vibration of circular arches", *Journal of the Engineering Mechanics Division,* **98**(EM2), 311-329.
Volterra, E. and Morell, J. D. (1961), "Lowest natural frequencies of elastic hinged arcs", *Journal of the Acoustical Society of America,* **33**, 1787-1790.
Wang, T. M. (1972), "Lowest natural frequency of clamped parabolic arcs", *Journal of the Structural Division,* **98**(ST1), 407-411.
Wang, T. M. and Moore, J. A. (1973), "Lowest natural extensional frequency of clamped elliptic arcs", *Journal of Sound and Vibration,* **30**, 1-7.
Wung, S. J. (1967), "Vibration of hinged circular arches", *Master's Thesis*, Rice University, Houston, Texas.